Effects of porous walls on near-wall supersonic turbulence

Yongkai Chen[*]

School of Mechanical Engineering, Purdue University, West Lafayette, Indiana 47906, USA

Carlo Scalo

School of Mechanical Engineering and School of Aerospace Engineering, Purdue University,
West Lafayette, Indiana 47906, USA

We have investigated the effects of the wall permeability on the isothermal-wall supersonic channel flow turbulence. The study is conducted via large-eddy simulations (LES) based on the sub-grid-scale closure proposed by Vreman [Phys. Fluids **16**, 3670 (2004)]. The effects of the wall porosity are modeled via the application of a time-domain impedance boundary condition (TDIBC), which accurately imposes the complex acoustic wall impedance. Bulk Mach numbers of $M_b = 1.50$ and 3.50 are selected, with bulk Reynolds numbers chosen to ensure the same semilocal friction Reynolds number of $\mathrm{Re}_\tau^* \approx 220$. A three-parameter impedance model is used with resonating frequency tuned to the time scales of the energy containing eddies, with wall acoustic resistances $R = 0.50, 1.00, \infty$, ranging from the most permeable to impermeable, respectively. It is found that only cases with $R = 0.50$ yield significant changes in the near-wall turbulence structures, which include a deviation from the linear relation of mean velocity and normalized wall distance in viscous sublayer, and increase in the mean wall-shear stress, as well as a strong increase in both turbulent kinetic energy (TKE) production and dissipation near the wall primarily due to large contribution coming from the instability waves triggered by the permeability. Such waves are found to be confined in the first 10% of the channel half-height near the impedance boundary, creating local circulation zones separated by regions of flow entrainment. It is found that for a given R, the waves are more confined as the Mach number increases. For pressure-related terms, the complex impedance wall effects changes the role of pressure diffusion term in the budget the most, making it responsible for the transport toward the wall, opposite to what is observed in impermeable wall cases. The confined waves also enhance the sink/source effect of the pressure strain term in budget of Reynolds normal stresses, leading to a redistribution of normal stresses.

I. INTRODUCTION

Porous media find widespread applications in aeronautical engineering for noise reduction and passive flow control. Performing high-fidelity numerical simulations including the flow in the pore space requires demanding effort in grid generation and high computational cost associated with the small grid size. When the effect of wall porosity is acoustic in nature, one solution is the mathematical imposition of a complex impedance $\widehat{Z}(\omega)$ at the interface between the flow domain

---

*chen1305@purdue.edu

and the porous media denoted as impedance surface. The impedance $\widehat{Z}(\omega)$ takes the form [1]

$$\widehat{Z}(\omega) = \frac{1}{\rho_s a_s} \frac{\widehat{p}(\omega)}{\widehat{\boldsymbol{v}}(\omega) \cdot \boldsymbol{n}} = R(\omega) + iX(\omega), \tag{1}$$

where ω is the angular frequency; $\widehat{p}$ and $\widehat{\boldsymbol{v}}$ are the Fourier transform of the pressure and velocity fluctuations, respectively; $\boldsymbol{n}$ is the unit vector normal to the impedance surface pointing away from the flow domain; ρ_s is the base density and a_s is the base speed of sound, both of which are taken at the impedance surface; i is the imaginary unit $i = \sqrt{-1}$. The impedance itself is a complex number, with the real part $R(\omega)$ and imaginary part $X(\omega)$ called resistance and reactance, respectively. A boundary condition that imposes the complex impedance $\widehat{Z}(\omega)$ is referred to as the impedance boundary condition (IBC). Such IBC formulation assumes linear wave propagation dynamics within the porous media and at the interface with the flow. To implement IBCs in time-domain based flow solvers a time-domain equivalent of Eq. (1), which appears in the form a convolution integral, must be numerically implemented at the impedance surface. Such boundary conditions are called time-domain impedance boundary conditions (TDIBCs). Constraints including passivity, reality, and causality must be honored by the TDIBC implementation to accurately predict the correct physics and to ensure numerical stability, as stated by Rienstra [2] and summarized by Douasbin *et al.* [3]. Tam and Auriault [4] proposed a three-parameter impedance model obtained by fitting experimental data from a typical acoustic liner in the frequency domain. A set of time-domain ODEs were derived directly from it. This type of TDIBC is proved to be well posed provided the imaginary part of the impedance has either nonnegative mass-like reactance or negative spring-like reactance (while using the $e^{-i\omega t}$ convention for Fourier transform). Later, Fung and Ju [5] proposed a TDIBC methodology based on the residue theorem. In this method, the time-domain convolution integral derived from Eq. (1) is evaluated numerically through the trapezoidal rule. However, this formulation is limited to second order accuracy in time. Dragna *et al.* [6] proposed the adoption of auxiliary differential equations (ADE) method for implementing TDIBC, which was originally developed in the field of electromagnetism [7]. With the ADE method, the convolution integral is converted into a set of ODEs with respect to two auxiliary variables, which can be advanced in time with the same time marching technique as the flow solver. Other TDIBCs methods based on different techniques such as z transform [8,9] and characteristic-based formulation [10–12] are also available in the literature. Readers are encouraged to consult the references for more details.

Researchers have applied TDIBCs to help investigate the effect of porous media on a fully subsonic turbulent flow field. For example, Jiménez *et al.* [13] performed Direct Numerical Simulations (DNS) of incompressible turbulent channel flow over one porous wall, in which the boundary conditions are those of purely real impedance, i.e., $v' = -\beta p'$ where β is the porosity coefficient. It was found that permeability significantly alters near-wall turbulence. Local blowing and suction regions have been identified, which on average increase the mean wall-shear stress. Scalo *et al.* [14] conducted a series of numerical experiments of compressible turbulent channel flow over complex wall impedance, using Fung and Ju's TDIBC technique and the three-parameter impedance model with the resonating frequency tuned to the most energetic frequency in the flow. The study spans a flow regime from nearly incompressible ($M_b = 0.05$) to low subsonic ($M_b = 0.5$). Spanwise rollers, exhibiting Kelvin-Helmholtz-type behavior, are found to replace the typical streamwise streaks. These structures are confined in a so-called resonating buffer layer—replacing the classic impermeable buffer layer—and change only the near-wall turbulent structures, as in flow over canopies. Later, [15] performed simulations of a similar flow with the same impedance model, but with the TDIBC formulation proposed by Ref. [4]. The flow conditions were at $M_b = 0.3$, with one case being $M_b = 0.4$, and with various selections of the resonating frequency. Results have shown that the spanwise coherence of the rollers gradually disappear as the resonating frequency is tuned beyond the characteristic flow frequency. All the aforementioned work focus on incompressible or subsonic compressible flow. The current work is motivated by the increasing attention to the application of porous media/coatings in high-speed flow, as well as the desire by the authors to
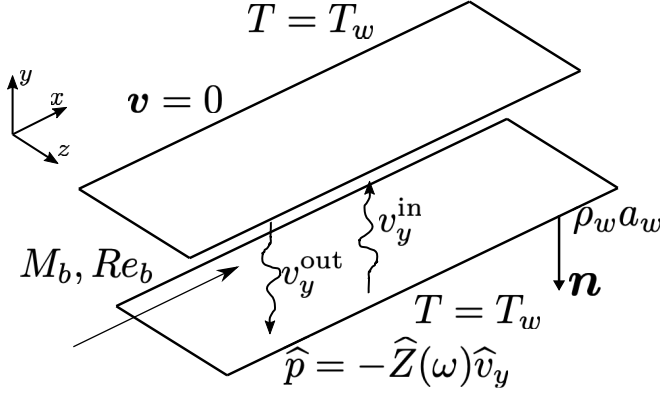
FIG. 1. Sketch of the flow setup for turbulent channel flow over one permeable wall. The negative sign in the impedance boundary condition comes from the convention of the outward-facing normal $\boldsymbol{n}$ [see Eq. (1)].

extend the work by Scalo *et al.* [14] to the supersonic and hypersonic regime. The effect of such surfaces on the high-speed near-wall turbulence is of great interest. To the authors' knowledge, there is no existing published work about their applications in high-speed turbulent flows. This paper and its companion publication [16] pioneer such investigation. The paper is organized as follows: Section II describes the flow problem, Sec. III provides the numerical setup, results are discussed in Secs. IV–VI, and conclusions are provided in Sec. VII.

II. PROBLEM FORMULATION

In this paper, large-eddy simulations (LES) of fully developed turbulent channel flow with isothermal walls are performed. The top wall is kept impermeable for all cases, while the bottom wall is allowed to have various degrees of permeability modeled by time-domain impedance boundary conditions. The flow setup is shown in Fig. 1. For clarity, the coordinate $(x, y, z) = (x_1, x_2, x_3)$ represent the streamwise, wall-normal, and spanwise directions, respectively. The reference parameters are the channel half-height δ, speed of sound at the wall a_w, wall temperature T_w, and bulk density $\rho_b = \langle \rho \rangle_V$, where the brackets $\langle \cdot \rangle_V$ indicate the volumetric-average operator. The bulk Reynolds number is then defined as

$$\mathrm{Re}_b = \frac{\rho_b U_b \delta}{\mu_{\mathrm{ref}}}, \tag{2}$$

where $U_b = \langle \rho u_1 \rangle_V / \rho_b$ is the density weighted bulk velocity, also yielding the bulk Mach number $M_b = U_b / a_w$; μ_{ref} is the dynamic viscosity taken at the wall. In the current work, the bulk Mach number M_b is chosen as $M_b = \{1.50, 3.50\}$. Different bulk Reynolds numbers Re_b are selected so that all Mach number cases share a similar viscous Reynolds number $\mathrm{Re}_\tau^* \approx 220$, that is, the semilocal viscous Reynolds number accounting for variable density effects [17] present in this flow.

The simulations are performed by solving the compressible Navier-Stokes equations:

$$\frac{\partial \rho}{\partial t} + \frac{\partial \rho u_j}{\partial x_j} = 0, \tag{3}$$

$$\frac{\partial \rho u_i}{\partial t} + \frac{\partial \rho u_i u_j}{\partial x_j} = -\frac{\partial p}{\partial x_i} + \frac{\partial \tau_{ij}}{\partial x_j} + \rho f_i, \tag{4}$$

$$\frac{\partial \rho E}{\partial t} + \frac{\partial \rho u_j E}{\partial x_j} = -\frac{\partial p u_j}{\partial x_j} + \frac{\partial (u_k \tau_{kj} - q_j)}{\partial x_j} + \rho f_j u_j. \tag{5}$$

Here τ_{ij} is the stress tensor given by

$$\tau_{ij} = (\mu + \mu_{\text{sgs}})\left(\frac{\partial u_i}{\partial x_j} + \frac{\partial u_j}{\partial x_i} - \frac{2}{3}\delta_{ij}\frac{\partial u_k}{\partial x_k}\right), \tag{6}$$

with the subscript "sgs" denoting sub-grid-scale (SGS) model terms. Note that a repeated i index implies the summation when used as a subscript, while used in equations such as Eq. (1) it indicates the imaginary unit. The heat flux vector q_j is defined as

$$q_j = -C_p\left(\frac{\mu}{\text{Pr}} + \frac{\mu_{\text{sgs}}}{\text{Pr}_{\text{sgs}}}\right)\frac{\partial T}{\partial x_j}, \tag{7}$$

where C_p is the heat capacity at constant pressure and $\text{Pr} = 0.72$ is the Prandtl number. The turbulent Prandtl number Pr_{sgs} is chosen to be 0.90. The ideal gas constitutive relation $p = \rho R_{\text{gas}}T$ is used with R_{gas} being the gas constant. The power law $\mu/\mu_{\text{ref}} = (T/T_{\text{ref}})^n$ is assumed for dynamic viscosity with $n = 0.76$. The eddy viscosity model by Vreman [18] is used as the turbulence closure.

To drive the flow, a uniform external body force f_1 in streamwise direction is dynamically adjusted to maintain the desired bulk mass flow rate. Its time average reads

$$\overline{f}_1 = \frac{\tau_w}{\delta\rho_b}, \tag{8}$$

where τ_w is the mean wall shear stress. For all simulations, periodic boundary conditions are used in streamwise and spanwise directions. For wall boundaries, the conditions are given as

$$u_1 = u_3 = 0, \tag{9a}$$

$$\begin{cases} u_2 = 0, & \text{impermeable,} \\ \hat{p} = \rho_w a_w \widehat{Z}(\omega)\hat{v}\cdot\boldsymbol{n}, & \text{permeable,} \end{cases} \tag{9b}$$

$$T = T_w, \tag{9c}$$

where $T_w = 1$ and $a_w = 1$ based on current normalization. For both permeable and impermeable walls, no-slip conditions are used for the tangential velocity components. One underlying assumption is that the orifice size of a corresponding physical array of Helmholtz resonators in the current setup is very small compared to the channel half height δ, and thus yields negligible tangential velocities, as also assumed for other types of porous walls used in high-speed flow applications [19]. Appendix A provides an analysis of the range of pore sizes relative to the boundary layer thickness typically found in high-speed flow conditions, supporting such assumption. For purely impermeable walls, the no-penetration condition is adopted (i.e., infinite impedance), while for permeable walls, TDIBC is applied with prescribed finite wall impedance $\widehat{Z}(\omega)$. Note that for the permeable wall simulations, the net mass flux across the impedance boundary is not enforced to be numerically zero. To prevent the occurrence of spurious net mass accumulation or leak in the channel, the surface-average mass flux through the impedance boundary is calculated at each sub-timestep, and converted into a density weighted wall-normal velocity $\tilde{v} = \overline{\rho v}/\overline{\rho}$. Such velocity is then subtracted from the instantaneous vertical velocity at the impedance boundary, ensuring a zero net mass flux through the whole impedance boundary at each sub-timestep. More details on the TDIBC implementation are discussed in the next two subsections.

A. TDIBC based on ADE method

Instead of directly using $\widehat{Z}(\omega)$, the TDIBC in the current work relies on the time-domain expression of the complex wall softness coefficient $\widehat{S}(\omega)$ defined as

$$\widehat{S}(\omega) = \frac{2}{1 + \widehat{Z}(\omega)}. \tag{10}$$

Its relation with the complex wall reflection coefficient, $\widehat{R}(\omega)$ is simply $\widehat{S}(\omega) = \widehat{R}(\omega) + 1$. The reflection coefficient $\widehat{R}(\omega)$ directly measures the magnitude and phase changes between the incident and the reflected waves, with values of $-1, 0, +1$ corresponding to surfaces of hard reflection, no reflection and pressure-release conditions, respectively. The complex wall-softness shares similar properties and relates the (flow) domain-leaving wave, $\hat{v}_n^{\text{out}}(\omega)$, to the domain-entering wave, $\hat{v}_n^{\text{in}}(\omega)$, both normal to the bottom-wall impedance surface, via

$$\hat{v}_n^{\text{in}}(\omega) = [\widehat{S}(\omega) - 1)]\hat{v}_n^{\text{out}}(\omega). \tag{11}$$

The time-domain expressions for such waves at the bottom boundary (with $\boldsymbol{n}$ for the bottom boundary pointing downwards) read

$$v_n^{\text{out}}(t) = v_n'(t) - \frac{p_w'(t)}{\rho_w a_w}, \tag{12a}$$

$$v_n^{\text{in}}(t) = v_n'(t) + \frac{p_w'(t)}{\rho_w a_w}, \tag{12b}$$

where $p_w'(t)$ is the pressure fluctuation at the wall. Such local recasting of the fluctuating field is consistent with Poinsot and Lele [20]'s characteristic boundary condition approach for the compressible Navier-Stokes equations. The impedance is here after assumed to act on only the acoustic waves.

The time-domain equivalent form of Eq. (11) is

$$v_n^{\text{in}}(t) = -v_n^{\text{out}}(t) + \int_{-\infty}^{\infty} s(\tau) v_n^{\text{out}}(t - \tau) d\tau. \tag{13}$$

The goal of TDIBC methods is to evaluate this integral while ensuring the physical realizability of the boundary condition. It has been summarized by Rienstra [2] that physical realizability can be ensured by satisfying passivity, reality, and causality constraints. However, such constraints are derived based on $\widehat{Z}(\omega)$, i.e., the formulation in Eq. (1). When the characteristic form of the incoming and outgoing acoustic waves is used [Eq. (11)], the constraints, which should be applied on $\widehat{S}(\omega)$ to ensure a causal integral, read:

(1) *Passivity of the impedance boundary.* The acoustic power through the impedance surface must entail a net acoustic energy transfer outside of the domain. Suppose $\widehat{S}(\omega)$ can be written as a fractional function, i.e., $\widehat{S}(\omega) = \widehat{A}(\omega)/\widehat{B}(\omega)$, then such constraint requires

$$\Re\{\widehat{B}(\omega)\} \geqslant 1, \forall \omega \in \mathbb{R}, \tag{14}$$

which is equivalent to $\Re\{\widehat{Z}(\omega)\} \geqslant 0$ for all real ω.

(2) *Reality of the signals.* This guarantees the signals obtained in time-domain are purely real, resulting in

$$\widehat{S}(\omega) = \widehat{S}^{\star}(-\omega), \tag{15}$$

with $\star$ representing the complex conjugate.

(3) *Causality.* The state of the physical process at the current time should not depend on the information from future. This means that the contribution to the convolution integral in Eq. (13) due to $\tau < 0$ should be zero, hence $s(\tau) = 0$ for $\tau < 0$.

The TDIBC methodology adopted in the current work builds upon the auxiliary differential equation (ADE) method [6,7] as well as the recasting of $\widehat{S}(\omega)$ into the summation of partial fractions using its residues, $\mu_k = a_k + ib_k$, and poles, $p_k = c_k + id_k$, which is interpretable as the linear superposition of n_0 causal harmonic oscillators [21],

$$\widehat{S}(\omega) = \sum_{k=1}^{n_0} \left(\frac{\mu_k}{i\omega - p_k} + \frac{\mu_k^{\star}}{i\omega - p_k^{\star}} \right). \tag{16}$$

With such form, the reality constraint is automatically satisfied. The causality constraint requires the real part of the poles p_k to be negative, i.e., $c_k \leqslant 0$, which then yields the expression in the time domain,

$$s(t) = \sum_{k=1}^{n_0} \left(\mu_k e^{p_k t} + \mu_k^{\star} e^{p_k^{\star} t} \right) H(t),$$

(17)

where $H(t)$ is the Heaviside function resulting from the inverse transform. Note that this mathematical form only implies one-way causality, consistent with the fact that the acoustic characteristic reflected off the impedance boundary $v_n^{\text{in}}(t)$ is dependent, in a one-way fashion, on $v_n^{\text{out}}(t)$, impinging on the impedance boundary.

A new set of auxiliary variables is then defined,

$$\psi_k^{(1)}(t) = \int_0^t 2a_k e^{c_k(t-\tau)} \cos[d_k(t-\tau)] v_n^{\text{out}}(\tau) d\tau,$$

(18)

$$\psi_k^{(2)}(t) = \int_0^t 2b_k e^{c_k(t-\tau)} \sin[d_k(t-\tau)] v_n^{\text{out}}(\tau) d\tau,$$

(19)

and the domain-leaving, $v_n^{\text{out}}(t)$, and domain-entering, $v_n^{\text{in}}(t)$, waves can be related via

$$v_n^{\text{in}}(t) = -v_n^{\text{out}}(t) + \sum_{k=1}^{n_0} 2\left[a_k \psi_k^{(1)}(t) - b_k \psi_k^{(2)}(t) \right],$$

(20)

with $\psi_k^{(1)}(t)$ and $\psi_k^{(2)}(t)$ governed by the ODEs

$$\frac{d\psi_k^{(1)}(t)}{dt} = c_{k-1} \psi_k^{(1)}(t) - d_{k-1} \psi_k^{(2)}(t) + v_n^{\text{out}}(t),$$

(21)

$$\frac{d\psi_k^{(2)}(t)}{dt} = c_{k-1} \psi_k^{(2)}(t) + d_{k-1} \psi_k^{(1)}(t),$$

(22)

where a_k, b_k, c_k, d_k are the real and imaginary parts of the residues μ_k and poles p_k, as stated above. Such ODEs can then be advanced with the same temporal scheme as the main flow solver and boundary conditions can be applied by solving for v_n and p'_w from Eq. (12). A more generalized impedance boundary condition could be developed to account for vortical and entropy mode impedances (see Suzuki and Lele [22]). This effort is out of scope of the current paper and it would also raise issues of practical realizability of such generalized boundary condition.

B. The three-parameter impedance model

In the present work, the three-parameter impedance model proposed by Tam and Auriault [4] is adopted:

$$\widehat{Z}(\omega) = R + i(X_+ \omega - X_{-1} \omega^{-1}),$$

(23)

which can be shown to be equivalent to a single-pole Helmholtz oscillator [21]. Here R, X_+, X_{-1} are acoustic resistance, acoustic mass-like reactance, and acoustic spring-like reactance, respectively. Note that unless otherwise indicated, the time harmonic convention $e^{+i\omega t}$ is assumed in this paper, as opposed to Tam and Auriault [4] who adopted the $e^{-i\omega t}$ convention. The model in Eq. (23) entails a frequency-selective acoustic permeability, which can be tuned to a characteristic frequency ω_{res} given by

$$\omega_{\text{res}} = \sqrt{\frac{X_{-1}}{X_{+1}}}.$$

(24)

In this paper, an equivalent set of three parameters R, ω_{res} and ζ are used where ζ is the damping ratio defined as

$$\zeta = \frac{1 + R}{2\omega_{\text{res}}X_{+1}}. \tag{25}$$

The impedance model in Eq. (23) can then be recast into the fully dimensionless form

$$\widehat{Z}\left(\frac{\omega}{\omega_{\text{res}}}\right) = R + i\frac{R + 1}{2\zeta}\left[\frac{\omega}{\omega_{\text{res}}} - \frac{\omega_{\text{res}}}{\omega}\right]. \tag{26}$$

With the above form of impedance and its connection to $\widehat{S}(\omega)$, one can show that the three aforementioned constraints in Sec. II A requires (for an underdamped system)

$$\begin{cases} R \geqslant 0, & \text{passivity}, \\ \zeta \in (0, 1), & \text{causality}, \end{cases} \tag{27}$$

where the reality constraint Eq. (15) is automatically satisfied. Preliminary results have shown that a very low resistance R—or, equivalently, very high permeability—could cause high amplitude instability waves in the flow and thus impose severe constraints on the allowable Courant-Friedrichs-Lewy (CFL) numbers. Hence, values of R are selected as $R = 0.50, 1.00, \infty$ for both Mach numbers, where the infinite value of R corresponds to impermeable wall conditions. A value of $\zeta = 0.5$ is selected for all permeable wall simulations. The impedance boundary in the current work is designed to react to the frequencies of energy containing eddies of the overlying turbulent flow, which yields the tuning condition

$$\omega_{\text{res}} = 2\pi U_b/\delta. \tag{28}$$

consistent with the approach followed by Scalo *et al.* [14]. It should be noted that the TDIBC based on such three-parameter impedance model could be implemented in a simpler and more straightforward way, such as the method used by Ref. [23]. In the current work, however, we have chosen to adopt a general approach that can allow for any realizable form of impedance to be applied as a boundary condition in a high-fidelity compressible-flow calculation.

III. NUMERICAL SETUP AND FLOW CONDITIONS

The compressible Navier-Stokes equations with prescribed boundary conditions are solved via a six-order compact finite differencing code originally developed by Ref. [24] and now under continued development at Purdue. The code implements grid transformation to allow the problem to be solved on curvilinear grids. A semi-implicit temporal scheme is used to alleviate the constraints in CFL numbers imposed by strong vertical velocities near the permeable wall, and it has been developed based on previously established fully implicit methods [24–27] and the explicit Runge-Kutta (RK) scheme used by Ref. [28]. Only the wall normal derivative terms are treated implicitly and are solved within each Runge-Kutta substep. The approximate factorization allows the resulting matrix-inversion problem to be solved iteratively with relatively low cost by using alternating direction implicit (ADI) sweeping. Three subiterations have been proven to be sufficient to ensure convergence at each RK substep. The validation of such scheme can be found in the reference [16].

The flow conditions and the grid size of all cases presented are listed in Table I. The domain size for cases with impermeable walls are both $L_x \times L_y \times L_z = 12\delta \times 2\delta \times 4\delta$, while the rest of the cases with finite R can be appropriately simulated in a shorter domain in the streamwise direction, $L_x \times L_y \times L_z = 8\delta \times 2\delta \times 4\delta$, as proven by the two-points correlations given in Appendix B. The number of grid points is chosen so that the grid spacing is fine enough to resolve the near-wall event induced by the impedance wall. A grid sensitivity study has been performed for the case with most energetic response, i.e., $M_b = 3.50$, $R = 0.50$, and the results are given in Appendix C. The validation of TDIBC implementation can be found in the companion publication [16]. In Table II

TABLE I. Flow conditions, impedance parameters, and number of grid points for all the LES cases. Cases run at $M_b = 1.50$ and 3.50 are hereafter labeled with the "(I)" and "(II)" Roman numerals, respectively.

Group	M_b	Re_b	R	$L_x \times L_y \times L_z$	$N_x \times N_y \times N_z$
(I)	1.50	5000	∞	$12\delta \times 2\delta \times 4\delta$	$160 \times 192 \times 120$
			1.00	$8\delta \times 2\delta \times 4\delta$	$128 \times 192 \times 128$
			0.50	$8\delta \times 2\delta \times 4\delta$	$128 \times 192 \times 128$
(II)	3.50	10000	∞	$12\delta \times 2\delta \times 4\delta$	$400 \times 256 \times 240$
			1.00	$8\delta \times 2\delta \times 4\delta$	$270 \times 256 \times 240$
			0.50	$8\delta \times 2\delta \times 4\delta$	$340 \times 300 \times 300$

the grid resolution is reported in terms of the plus units, along with the time-step and CPU hours per flow-through time. Note that due to the asymmetry in the boundary conditions, data based on top and bottom wall statistics are given separately.

IV. MEAN VELOCITY AND REYNOLDS STRESSES

In this section, some of the first and second-order mean flow statistics are reported. Unless otherwise stated, the Favre averaging [30] is used. The Favre-averaged mean value of a quantity ϕ is denoted by $\widetilde{\phi}$ and the fluctuation by ϕ'', while for Reynolds average $\overline{\phi}$ and ϕ' are used to represent the mean and the fluctuation part, respectively. Figure 2 shows the transformed mean streamwise velocity profile as well as the Favre-averaged Reynolds stresses $\widetilde{u_i'' u_j''}$. The transformation applied to the mean velocity is the one proposed by Ref. [29] for compressible wall-bounded turbulence, denoted as U^{TL} (and hereafter referred to as TL transformation), which has been shown to collapse the mean velocity profile for Mach number up to 4.0 for compressible turbulent channel flows.

The TL transformation naturally yields the semilocal wall normal coordinate y^* defined as [17]

$$y^* = \frac{\overline{\rho} u_\tau^* y}{\overline{\mu}}, \quad u_\tau^* = \sqrt{\tau_w / \overline{\rho}}, \tag{29}$$

where $\overline{\rho}$ and $\overline{\mu}$ are local flow density and dynamic viscosity averaged in time and homogeneous directions; τ_w is the mean wall shear stress. The corresponding normalization of the Reynolds stress is given as $\overline{\rho u_i'' u_j''} / \tau_w$. For reference, the compressible channel flow data by Ref. [31] ($M_b = 1.50$, $\mathrm{Re}_b = 5000$) and the incompressible channel flow data from Ref. [32] are also included.

TABLE II. Grid resolutions in wall units and percentage increase in the wall shear stress for the permeable-wall LES cases. Top and bottom wall statistics are reported separately. The increasing dash spacing in the line style indicates increasing wall permeability. The time step and the CPU hours per flow-through time are also reported.

| Group	M_b	R	Line style	Δx^+	$\Delta y_{\min}^+$	Δz^+	$\Delta \tau_w(\%)$	Δx^+	$\Delta y_{\min}^+$	Δz^+	$\Delta \tau_w(\%)$	Δt	CPU hours/ flow-through time
				Bottom				**Top**					
(I)	1.50	∞	——	25.37	0.14	11.30	0.00	25.23	0.14	11.24	0.00	2×10^{-4}	16 457
		1.00	------	21.53	0.14	10.77	2.33	20.94	0.14	10.47	+2.18	2×10^{-4}	16 384
		0.50	- - - -	22.87	0.15	11.44	18.02	21.40	0.14	10.70	+4.42	2×10^{-4}	16 384
(II)	3.50	∞	——	28.85	0.30	16.06	0.00	29.22	0.30	16.26	0.00	2×10^{-4}	82 285
		1.00	------	30.22	0.32	17.01	12.35	29.38	0.31	16.53	+3.35	1×10^{-4}	87 711
		0.50	- - - -	23.81	0.27	13.50	10.93	23.00	0.26	13.04	+0.62	1×10^{-4}	137 143
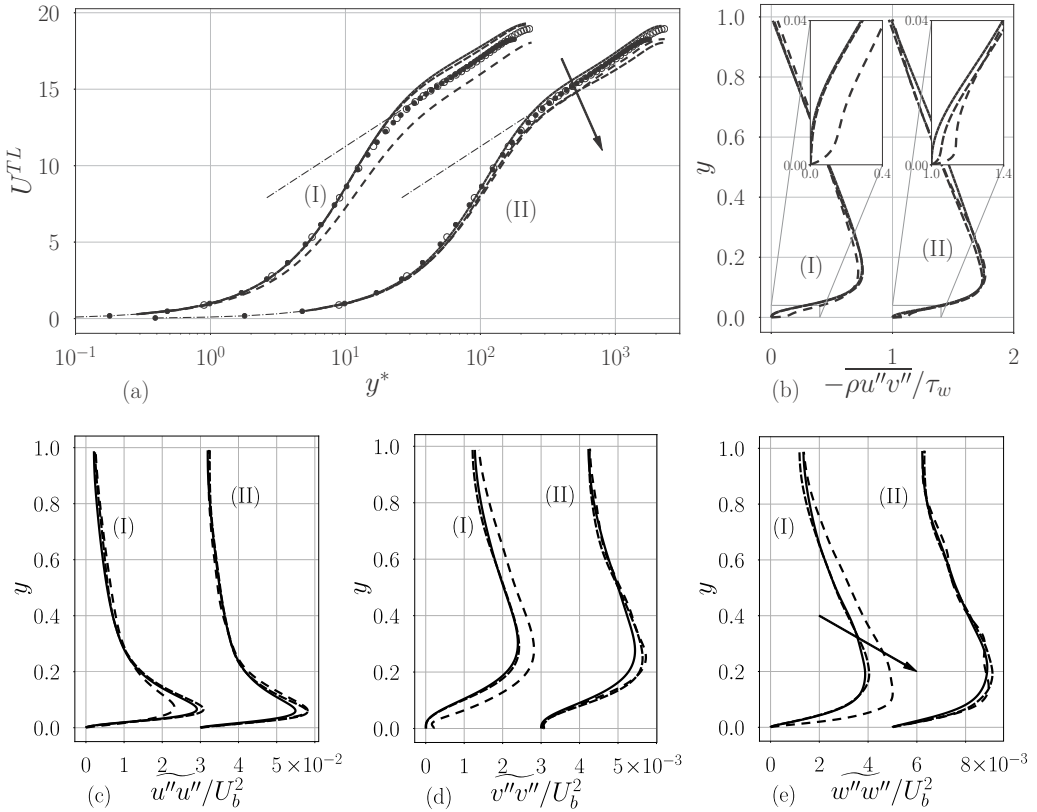
FIG. 2. First and second-order flow statistics: (a) TL-transformed mean streamwise velocity profile [29]. The dashed-dotted line represents the reference log-law $U^{TL} = 2.5\ln y^* + 5.5$ and the linear law (below $y^* = 5$); (b) Reynolds shear stress normalized by mean wall shear; (c)–(e) Reynolds normal stresses normalized by U_b^2. The line spacing in the plot increases with an increasing permeability (decreasing resistance R). Arrows indicate direction of increasing permeability.

For the LES impermeable wall cases, the near-wall profiles agree well with reference data. The case at $M_b = 1.50$ starts to see an overshoot beyond $y^* \approx 15$, while case with the higher Mach number shows good agreement across the whole channel. With wall permeability, the mean velocity profile starts to deviate from its impermeable reference as shown in Fig. 2(a). For both Mach numbers, the effect of wall permeability is not apparent at $R = 1.00$. As R decreases to the value of 0.50, the mismatch appears early in the viscous sublayer region and continues all the way to the channel center. At such low values of wall acoustic resistance, the typical viscous sublayer scaling, or $U^{TL} \approx y^*$, is no longer followed. For this reason, the value of y^* loses its correlation to a specific state of wall-bounded turbulence. As a result, most of the statistics shown later will simply use the wall normal coordinate y made dimensionless with the channel semi-height δ. The high near-wall velocity gradient indicates the increase in the mean wall shear stress compared to the impermeable wall baselines, whose values are also reported in terms of percentage increase $\Delta \tau_w$ in Table II. Except for the one with $R = 1.00$ at $M_b = 1.50$, all other cases show at least 10% of enhancement in the mean wall shear stress. The Reynolds shear stress $-\overline{\rho u'' v''}/\tau_w$ reflects the near-wall changes more clearly and is given in Fig. 2(b). A local peak of $-\overline{\rho u'' v''}/\tau_w$ is observed below $y = 0.02$ (see the inset view), which means a stronger correlation between fluctuations in streamwise and wall normal velocity components at this location, and thus an enhancement in

the convective momentum transfer in the near-wall region. Again, such enhancement has not been observed in the low permeability case at low Mach number with high resistance.

Figures 2(c) and 2(e) demonstrate the normal Reynolds stresses, which are normalized by U_b^2 to allow for an easier comparison. A redistribution of the turbulence intensities has been observed due to wall porosity, which also varies with Mach numbers. Typically the no-slip impermeable wall conditions lead to a two-component nature of turbulent channel flow in the near-wall region—the vertical component $\widetilde{v''v''}$ grows roughly as y^4 while $\widetilde{u''u''}$ and $\widetilde{w''w''}$ as y^2, resulting in $\widetilde{v''v''}$ approaching zero at the wall much faster than the other two components [33]. In addition, $\widetilde{u''u''}$ is usually the largest component because of the fluctuation energy extraction from the mean stream-wise shear. The high resistance cases ($R = 1.00$) at both Mach numbers do not show significant differences with respect to the impermeable baseline cases, except for a slightly increase in the peak of $\widetilde{u''u''}$. For lower resistance $R = 0.50$ at low Mach number $M_b = 1.50$, a decrease is observed in $\widetilde{u''u''}$ in the near-wall region and the other two components exhibit enhancement in the lower half channel. However, when keeping the same resistance and increasing the Mach number, an increase in all stress components are observed. Nonzero values of $\widetilde{v''v''}$ are observed due to the nonzero transpiration velocity v' at the permeable wall. This redistribution of the normal stresses will be addressed with further details in Sec. VI B. The observation in the first and second-order mean statistics suggests that for cases with sufficiently high wall permeability, the near-wall turbulence structures might have been altered. The structural-wise changes are investigated in the next section.

V. NEAR-WALL TURBULENCE STRUCTURES

A. Streamwise traveling structures

The mean flow statistics indicates the possibility of the alterations in near-wall turbulence structures, which is confirmed in Fig. 3, where for cases with $R = 0.50$ the isosurface of Q criterion [34] are shown on top of contour of wall pressure fluctuations.

Groups of streamwise traveling structures are identified, which leave a coherent footprint of pressure waves on the wall surface. The characteristic wavelength of such structures is found to be $\lambda_x \approx 0.47$ for both Mach numbers. The velocity field obtained by subtracting the mean flow from the instantaneous field shows that such waves create localized circulation zones in regions of positive pressure fluctuation p', separated by flow entrainment region that brings the high momentum fluid toward the wall, which leads to a local increase of the wall shear stress. With the same $R = 0.50$, a discernible difference in the pressure pattern of $M_b = 1.50$ and $M_b = 3.50$ is observed. At $M_b = 3.50$, the wave structure is confined closer near the wall, with the high pressure blob more concentrated in a smaller region, as compared to the pattern at $M_b = 1.50$. In Ref. [14], the permeable walls in subsonic channel flows trigger Kelvin-Helmholtz type of instability, and result in a layer of spanwise rollers that disrupt the viscous sublayer. At that low Mach number, the characteristic length scale of the rollers was found to be $\lambda_x \approx 0.40$ with regions of flow entrainment and circulation zones of comparable size. In the current work a longer length scale of the instability is observed with $\lambda_x \approx 0.47$ and circulation regions are more extended than the entrainment region. As the Mach number increases, a deviation from spatially harmonic pattern is observed, with more localized and abrupt positive pressure fluctuations, indicating possible coupling with the overlying flow field, associated to a stronger flow response; For the lower Mach number case, the same value of dimensionless resistance ($R = 0.50$) yields a weaker response, which preserves its modal nature and hence likely decouples from the turbulence. This behavior might relate to the increasing temperature gradient as the Mach number increases in such type of flow, which requires further investigation in the future. For all Mach number cases, the observed waves are 'trapped' as shown in a companion work [16], in the sense of wave being confined near the impedance boundary but able to propagate along the boundary indefinitely. The same type of waves have been defined by Ref. [35] as "surface waves" when discussing waves confined close to an impedance lining in a duct with flow. However,
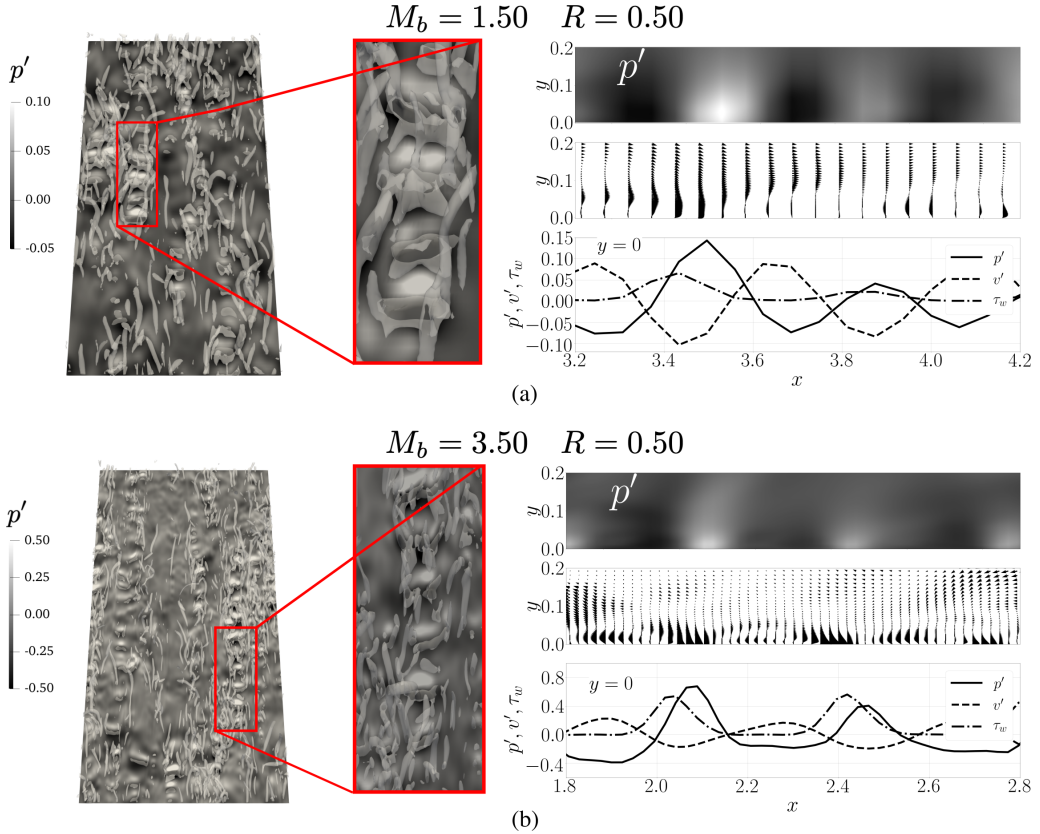
FIG. 3. Near-wall instability waves resulting from the interaction of the impedance wall and the overlying supersonic turbulent flow field. The cases presented are (a) $M_b = 1.50$, $R = 0.50$ and (b) $M_b = 3.50$, $R = 0.50$. In each subfigure, the following quantities are shown: Isosurface of Q criterion overlaid on the pressure fluctuation contour on the wall (left); spanwise slice of the pressure contour showing the characteristic wave length λ_x (top right); The vector plot of fluctuating velocity field (center right); Signals of wall normal velocity, pressure fluctuation and shear stress at $y = 0$ at the same spanwise slice (bottom right).

in acoustics the term "trapped" refers to a wave that is not able to escape a given region in any direction [36], and therefore the word "trapped" is avoided here for clarity.

B. Vorticity fluctuation intensity

The presented flow structures due to the response of permeable walls greatly affect the vorticity field near the wall. The normalized root-mean-square (RMS) vorticity components $\langle \omega_x \rangle^*_{\mathrm{rms}}$ are presented in Fig. 4. The superscript "∗" indicates the value that is normalized by the quantity $\mu_{\mathrm{ref}}/\tau_{w,R=\infty}$ taken from the baseline cases. The logarithm scale is used to emphasize the near-wall changes.

In all the cases presented, the wall normal component $\langle \omega_y \rangle^*_{\mathrm{rms}}$ does not experience obvious changes over various wall permeabilities except for the low resistance case at $M_b = 1.50$ in which an enhancement of $\langle \omega_y \rangle^*_{\mathrm{rms}}$ is shown below $y = 0.1$. The effect of wall permeability mainly exists in the other two components, $\langle \omega_x \rangle^*_{\mathrm{rms}}$ and $\langle \omega_z \rangle^*_{\mathrm{rms}}$. In a typical impermeable channel flow, clusters of streamwise streaks resides near the wall, which can be approximately visualized as streamwise aligned vortices. On the average, these streaks create a local maximum at $y \approx 0.1$ in $\langle \omega_x \rangle^*_{\mathrm{rms}}$ (roughly at $y^* = 24 \sim 25$ in an impermeable wall case), which corresponds to the averaged height of the
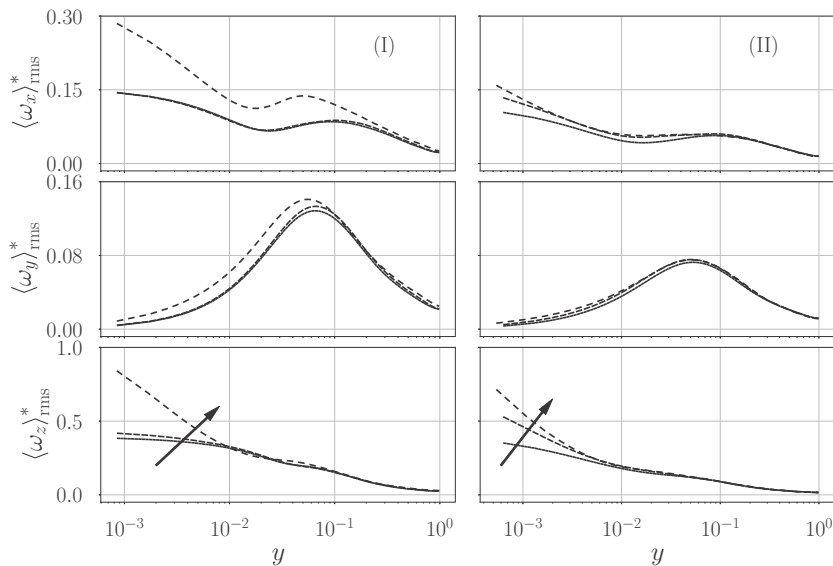
FIG. 4. Root-mean-square fluctuation vorticity components, normalized by μ_{ref} and the wall shear stress τ_w in the impermeable wall cases. The line spacing in the plot increases with an increasing permeability (decreasing resistance R), also shown by the arrow.

vortex centers [37]. Due to the no-slip condition in u and w, a maximum in $\langle\omega_x\rangle^*_{\text{rms}}$ is observed on the surface. The combined effect of streaks and no-slip conditions leads to a local minimum that is roughly at the edge of the pictured vortex structures. After applying the permeable wall condition, significant enhancement of $\langle\omega_x\rangle^*_{\text{rms}}$ is observed below $y = 0.2$ and the locations of the local maximum and minimum are shifted closer to the wall. The phenomenon of increasing $\langle\omega_x\rangle^*_{\text{rms}}$ is due to the entrainment effect of the wave structures as presented in Fig. 3, which is in fact a three-dimensional event as sketched in Fig. 5. While the high momentum fluid is entrained toward the wall, it is also found to be expelled to the cross direction. This leads to secondary flows that increase the component $\partial w'/\partial y$ and thus $\langle\omega_x\rangle^*_{\text{rms}}$. A cross-plane view of the flow field is shown in
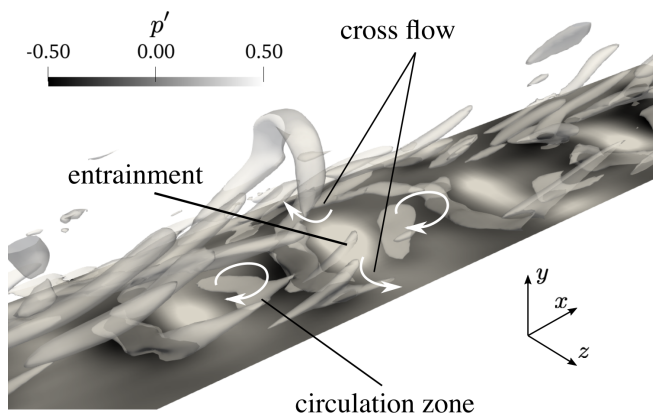

FIG. 5. A sketch of the flow pattern associated to wave-like structures showing the circulation zone, entrainment region and the resulting cross flow. The background isosurface plot is generated with the case $M_b = 3.50, R = 0.50$).
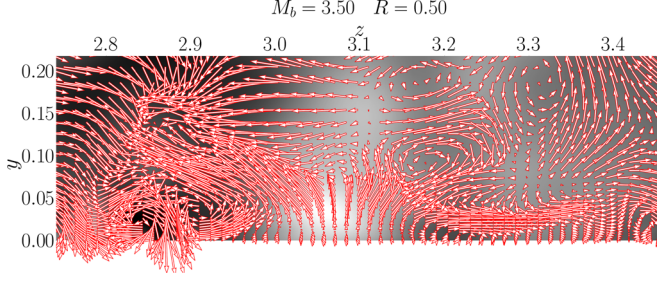
FIG. 6. Instantaneous flow field in the cross-plane (z-y plane) at the location of entrainment (positive pressure fluctuation) on top of the contour plot of pressure fluctuations, taken from the case $M_b = 3.50, R = 0.50$. The vector length is proportional to the in-plane velocity magnitude.

Fig. 6 for $M_b = 3.50, R = 0.50$, which clearly shows the cross flow on sides of the positive pressure fluctuation blob, where the flow entrainment is present. The effect of permeable walls on $\langle \omega \rangle^*_{z,\mathrm{rms}}$ is mainly confined below $y = 0.02$. Significance enhancement of the strength can be observed below $y = 0.01$, which tends to be the effect of circulation zones captured by Q criterion as spanwise "rollers" as previously shown in Fig. 3.

VI. TKE BUDGET ANALYSIS

In this section, parts of the budgets of turbulence kinetic energy (TKE) will be examined. The transport equation for TKE in compressible flows, including the SGS contribution, is given by

$$\overline{\rho}\frac{\partial k}{\partial t} + \overline{\rho}\widetilde{u}_j\frac{\partial k}{\partial x_j} = P^k - \epsilon + D^k + T^k + D^k_p + W^k + \Pi^k_p - \epsilon_{\mathrm{sgs}} + D^k_{\mathrm{sgs}}, \tag{30}$$

where $k = \frac{1}{2}\widetilde{u''_i u''_i}$ represents the TKE. Two groups of the terms on the right-hand side of TKE budget are selected for further examination:

(1) Group I: Production and dissipation

$$P^k = -\overline{\rho u''_i u''_j}\frac{\partial \widetilde{u}_i}{\partial x_j}, \quad \text{production,} \tag{31a}$$

$$\epsilon = \overline{\tau_{ji}\frac{\partial u''_i}{\partial x_j}}, \quad \text{resolved dissipation,} \tag{31b}$$

$$\epsilon_{\mathrm{sgs}} = \overline{\tau_{ji,\mathrm{sgs}}\frac{\partial u''_i}{\partial x_j}}, \quad \text{SGS dissipation.} \tag{31c}$$

(2) Group II: Pressure-related terms

$$D^k_p = -\frac{\partial \overline{p'u''_j}}{\partial x_j}, \quad \text{pressure diffusion,} \tag{32a}$$

$$W^k = -\overline{u''_i}\frac{\partial P}{\partial x_i}, \quad \text{pressure work,} \tag{32b}$$

$$\Pi^k_p = \overline{p'\frac{\partial u''_i}{\partial x_i}}, \quad \text{pressure dilatation.} \tag{32c}$$

Unless otherwise mentioned, all budget terms are normalized by the quantity $\tau_w U_b/\delta$ taken from the present impermeable-wall simulations. Some available reference data for impermeable-wall calculations [31] will also be included.
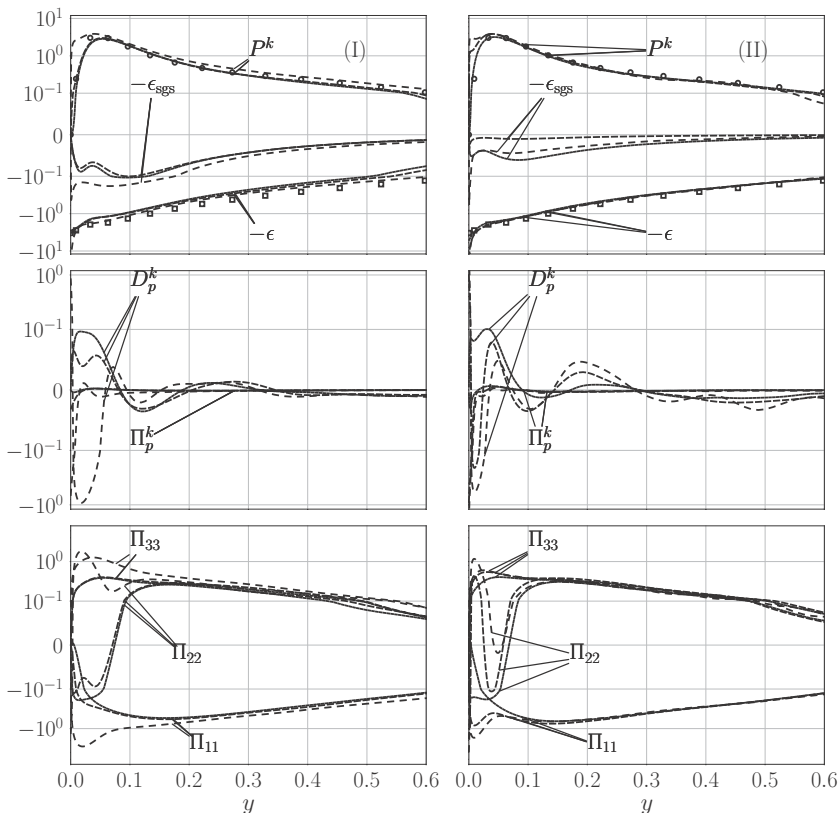
FIG. 7. Budgets terms below $y = 0.6$ for all simulations. Plots in the same column belong to the same Mach, indicated by labels "(I)" and "(II)." First row: Turbulence production, P^k, resolved dissipation, ϵ, and SGS dissipation, ϵ_{sgs}. Second row: pressure diffusion D_p^k and pressure dilatation Π_p^k. Third row: pressure-strain terms Π_{ii}, $i = 1, 2, 3$ as will be given in Eq. (37). The line spacing in the plot increases with an increasing permeability (decreasing resistance R). For the same Mach number, quantities in cases of various resistance R are normalized by values taken from impermeable wall simulations.

A. Group I: Production and dissipation

In this section the turbulent production P^k and resolved dissipation ϵ are examined. For completeness, the SGS dissipation ϵ_{sgs} is also included. All these terms are plotted in Fig. 7. The dissipation term can be further decomposed into a solenoidal part, ϵ_s, and a dilatational part, ϵ_d, where

$$\overline{\rho}\epsilon_s = \overline{\nu}\overline{\rho\omega_i''\omega_i''}, \quad \overline{\rho}\epsilon_d = \tfrac{4}{3}\overline{\nu}\overline{\rho u_{i,i}''u_{i,i}''}. \tag{33}$$

Their ratio, ϵ_d/ϵ_s, is (surprisingly) found to be negligible for all cases and is not included in Fig. 7. As expected, cases with $R = 1.00$ exhibit no significant differences in the budgets as compared to the baseline impermeable cases due to their relatively low permeability (or high resistance R). Effects on the budgets due to the permeability start to show in lower resistance cases with $R = 0.50$. Higher turbulent production is observed in the near-wall region, with peaks of production shifted closer to the wall; the fluid layer of high turbulent production also widens. The change in turbulent production agrees with the trend shown in the mean velocity and Reynolds-shear stress previously shown in Fig. 2. Exploiting the statistical homogeneity in the x and z directions the production term
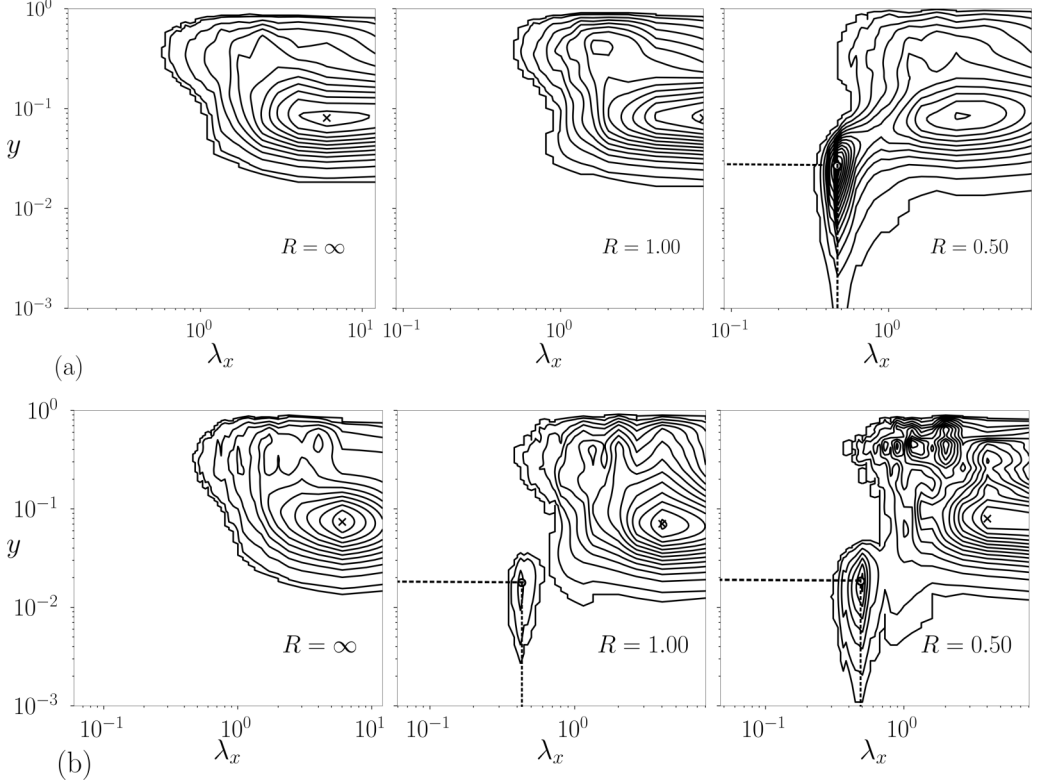
FIG. 8. Premultiplied production spectrum as a function of distance from the wall and streamwise wavelength at $M_b = 1.50$ (a) and $M_b = 3.50$ (b). The "x" symbols indicate the highest contribution to the production spectra. Dashed lines indicate the location and the wavelength of the contribution associated to the waves due to porous walls. The impermeable cases ($R = \infty$) have longer domains, hence the larger maximum λ_x.

reads

$$P^k = -\overline{\rho u'' v''} \frac{d\widetilde{u}}{dy}. \tag{34}$$

The reaction of the impedance wall to the overlying turbulence enhances the near-wall momentum transport, leading to higher wall shear (thus, high $d\widetilde{u}/dy$) and the Reynolds shear stress, which eventually results, in turn, in an enhancement of the turbulent production. Permeability also leads to a spike in dissipation, with a ten-fold increase at the wall as compared to impermeable baselines.

The observed changes in the TKE budgets are due to the instability wave pattern shown in Sec. V, which has been confirmed in the companion work [16] by showing the contribution of TKE production terms of different wavenumbers at different locations, though for slightly different wall permeabilities for each Mach number. Here the same methodology applied to the cases in this work, as shown in Fig. 8. The production spectrum reads

$$\widehat{P}^k = -\frac{1}{2}\left[\left\langle \Re\left\{\widehat{\rho u' v'}^{\star} \frac{d\widetilde{u}}{dy}\right\}\right\rangle_{z,t} + \left\langle \Re\left\{\widehat{\rho v' u'}^{\star} \frac{d\widetilde{u}}{dy}\right\}\right\rangle_{z,t}\right], \tag{35}$$

where the superscript * represents the complex conjugate of a quantity, and $\langle\cdot\rangle_{z,t}$ indicates an averaging operator in spanwise direction and time, and $\widehat{\cdot}$ the Fourier transform operator. This is similar to the method used by Ref. [38], with a modification to account for compressibility. It is also found that there is no significant difference between the two terms on the right-hand side of

Eq. (35) and thus an average operation is performed. Figure 8 shows the contour line plot of the premultiplied spectra

$$\widehat{\Phi}^*_{P^k,x} = \mathrm{Re}^*_\tau \kappa_x y \widehat{P}^k \mu / \tau^2_{w,R=\infty} \tag{36}$$

as a function of streamwise wavelength and distance from the wall, normalized by the shear stress of the reference impermeable cases.

At the lower Mach number with $R \geqslant 1.00$, most of the production is due to wavelengths $\lambda_x \geqslant 2.0$ and is concentrated in the region $y \in (0.05, 0.2)$, which roughly corresponds to $y^* \in (15, 50)$ of the impermeable wall case. As the resistance decreases to $R = 0.50$, the spectra exhibit the same pattern in the same region. However, a second region of high contribution has appeared in the range $y \in (0.01, 0.05)$, whose wavelength matches the length scale of the wave structure shown in Fig. 3. For $M_b = 3.50$, a similar behavior is observed and the second region also appears for the higher resistance case ($R = 1.00$). In either Mach number, the wave pattern of the instability observed in the flow is responsible for the enhancement in the near-wall production.

B. Group II: Pressure-related terms

All pressure-related terms in the TKE energy budgets are presented in this section, including pressure diffusion D^k_p and pressure dilatation Π^k_p. The term W^k_p, i.e., pressure work, is found to be negligible across the whole channel even with high wall permeability and it thus omitted from the plots. All these three terms are known to be small as compared to other terms in an impermeable wall channel flow. The pressure diffusion term D^k_p characterizes the TKE diffusion process caused by the fluctuating pressure, which tends to reduce the spatial heterogeneity in the TKE distribution. For an impermeable wall, a local maximum with a normalized value around 0.1 is observed near the wall at $y \approx 0.03$, serving as a gain term in the TKE budget, that is, TKE is transported into this region. The magnitude of D^k_p becomes negligible above $y = 0.2$. For permeable wall cases with $R = 1.0$ at $M_b = 1.50$, attenuation of the transport in the same region is observed, with no significant changes in other part of channel except for a nonzero value at the porous wall. At higher Mach number $M_b = 3.50$ for the same resistance, the peak changes sign and becomes negative, indicating TKE being diffused away from this region. Same negative peaks are observed at lower resistances $R = 0.50$ for both Mach numbers. In addition, a value around 1.0 is achieved on the wall surface as compared to zero for the impermeable wall. This behavior indicates that for the cases with the highest wall permeability, TKE is being diffused toward the porous surface by the pressure fluctuations. The value of pressure dilatation Π^k_p is negligible across the whole channel over an impermeable wall. The presence of an impedance wall merely results in a spike of negative pressure dilatation in the region $y \leqslant 0.02$. As shown in previous sections, a redistribution of energy in the normal components of Reynolds stresses is observed at both Mach numbers. It is therefore interesting to examine the pressure-strain term that is known to be responsible for TKE redistribution [33]. The pressure-strain term in normal components of Reynolds stresses can be obtained by deriving the corresponding transport equation given in Appendix D. The pressure-strain term then reads

$$\Pi_{ii} = \overline{2p' \frac{\partial u''_i}{\partial x_i}}, \quad i = 1, 2, 3. \tag{37}$$

Note that the summation over repeated indices is not used here, and i represents ith coordinate direction. The above terms are plotted in Fig. 7 for all cases presented. Π_{11} acts as a sink in the budget of $\widetilde{u''u''}$ across the whole domain, with a maximum peak achieved around $y = 0.08$ over an impermeable wall. The effect of the permeability is to further enhance the sink effect below $y = 0.2$, mainly for cases with $R = 0.50$ and permeable cases at $M_b = 3.50$. However for each Reynolds normal stress, it is the balance of its production, dissipation (components) and the pressure-strain that eventually determines the intensity, which is the reason that $\widetilde{u''u''}$ show slightly different behavior for different Mach numbers with resistance $R = 0.50$. The production of Π_{22} and Π_{33} are zero due to statistical homogeneity. For the rest two normal stresses, the production terms

are zero due to double statistical homogeneity. Permeability attenuates the sink effect of Π_{22} and enhance the source effect of Π_{33} in regions close to the wall, both of which lead to an increase in the respective normal stresses. This agrees with the observed redistribution of normal stresses in Fig. 2.

VII. CONCLUSION

To investigate the effect of porous media on supersonic turbulent flow field, large-eddy simulations of compressible turbulent channel flows over complex wall impedance at two bulk Mach numbers $M_b = 1.50, 3.50$ were carried out. The bulk Reynolds numbers of cases presented are adjusted to keep the viscous Reynolds number fixed around $\mathrm{Re}_\tau^* = 220$. A time-domain impedance boundary condition (TDIBC) based on auxiliary differential equation (ADE) method is applied to bottom wall of the channel, using a three-parameter model with a resonating frequency tuned to most energetic frequency in the turbulent channel flow. Two values of resistance $R = \{0.50, 1.00\}$, which is inversely proportional to the wall permeability at resonating frequency, are chosen for each Mach number. Results show that finite wall permeability has a significant effect on the near-wall turbulence with sufficiently low resistance value $R = 0.5$, while cases with $R = 1.0$ show no appreciable difference with the impermeable baseline cases. The typical law-of-wall is no longer followed with nonzero wall permeability and the deviation increases as the permeability increases. As compared to impermeable wall cases, higher wall-normal gradient of mean streamwise velocity is observed in permeable wall cases, indicating an increase in the mean wall shear stress. The phenomenon is due to the oscillatory wall normal velocity enhancing turbulent mixing close to the wall. Redistribution of Reynolds normal stresses are shown, with an increase in the components $\widetilde{v''v''}$ and $\widetilde{w''w''}$, and a drop in $\widetilde{u''u''}$ specifically to the case $M_b = 1.50, R = 0.50$, as a result of balancing among production, dissipation and pressure-strain terms.

The change in the mean flow statistics are directly related to the structural changes in the near-wall turbulence. Streamwise-traveling waves with a wavelength $\lambda_x \approx 0.47$ are captured by Q criterion in permeable wall cases, creating local circulations zones separated by entrainment that is directing the flow toward the wall. The analysis of TKE budgets shows that most of the effects are confined near the wall. The turbulence production is significantly enhanced below $y = 0.1$, with the most of contribution in this region coming from the aforementioned wave structures. The dissipation is also increased but its effect is mostly discernible on the wall surface. No obvious changes have been observed in dilatational dissipation. For other budget terms, pressure diffusion is the only one that is obviously altered: TKE is being diffused from where production reaches its maximum toward the wall at $R = 0.50$, opposite to the behavior of low permeability cases. It is also confirmed that the impedance wall significantly changes the pressure-strain terms in the budget of normal stresses, which eventually leads to the redistribution of TKE.

The only previous work applying IBCs in a hypersonic flow is limited to transitional flows [Fedorov *et al.* (2003); Sousa *et al.* (2019)]. With this paper we start to explore the possibility of controlling a high-speed fully developed turbulent flow. We have found the range of resistance values that yield an effect on the flow and have characterized what type of structural changes turbulence is experiencing as a result. This is the first step toward something more meaningful which might require optimization strategies applied to a variable surface impedance.

ACKNOWLEDGMENTS

TABLE III. Equivalent dimensional pore size d_{pore}, boundary layer thickness δ_{bl} (or channel half height) and characteristic resonant frequency f_{res} for current supersonic channel flow calculations and for two existing hypersonic flow cases.

Application	Mach	d_{pore}	δ_{bl}	f_{res}
Current Channel Flows Conditions	1.5	$\sim 100\,\mu\text{m}$	4.9 mm	228 kHz
	3.5	$\sim 100\,\mu\text{m}$	4.9 mm	531 kHz
Hypersonic Flow (T3-26 Tunnel) [19]	6.0	$100\,\mu\text{m}$	1 mm	225–375 kHz
Hypersonic Flow (HEG Tunnel) [41]	7.4	20–$100\,\mu\text{m}$	1 mm	300 kHz

APPENDIX A: ESTIMATION OF PORE SIZES IN HIGH-SPEED FLOWS

In Table III we analyze some realistic supersonic and hypersonic flow conditions, relating them to our permeable-wall channel calculations made dimensional by scaling the flow parameters to match HyShot II's combustor inlet at one working condition [39,40]. This results in dimensional values for effective pore diameters d_{pore} and resonating frequencies f_{res} of the impedance boundary condition that can be compared to realistic spatial and temporal scales.

The dimensional channel half height is chosen to be $\delta = 4.9$ mm, which can be interpreted as a reference boundary layer height. Varying the Mach number in the range $M = 1.5$–3.5 then results in a corresponding range of resonating frequencies $f_{\text{res}} = 228$–531kHz for the three-parameter IBCs used in our study. The frequencies are of the same order of magnitude as what naturally observed in the hypersonic flow cases mentioned in the table (T3-26 and HEG Tunnels). Assuming a wall porosity consistent with the adopted three-parameter model (i.e., an idealized Helmholtz resonator), the resulting resonating frequencies have been calculated via

$$f = \frac{a}{2\pi}\sqrt{\frac{A}{V_0\,\ell_{\text{eq}}}}, \tag{A1}$$

where a is the speed of sound, $A \sim d_{\text{pore}}^2$ the orifice's opening area, V_0 is the resonating cavity volume and ℓ_{eq} is the effective neck length. In the Hyshot II setup, the wall temperature is chosen as $T_w = 300K$ and the resulting speed of sound at the wall is $a_w \approx 347$ m/s. We assume V_0 and ℓ_{eq} share the common characteristic length scale ℓ_c given the typical structure of porous walls used in high-speed applications, resulting in $V_0 \sim \ell_c^3$ and $\ell_{\text{eq}} \sim \ell_c$. Choosing a pore diameter of $d_{\text{pore}} \sim 100\,\mu\text{m}$ (and hence $\ell_c \sim 100\,\mu\text{m}$), this results in the frequency range relevant to the first two cases of Table III. Another point is that values considered for the resistance (to be interpreted as the inverse of the wall permeability) are never lower than 0.5, further supporting the assumption of small pore size.

The small pore sizes reported here entail typical pore-size-to-Stokes-boundary-layer-thickness ratios of less than 0.1. This means that the wave-induced flow in the porous media is heavily viscously dominated, and the acoustic waves are strongly attenuated in the depth of the porous layer making nonlinear effects and slip-flow effects at the surface unlikely to be relevant.

With this pore size, one can do a back-of-the-envelope calculation about how many grid points would be required if the pores are fully resolved. Take the case $M_b = 3.50$ as an example whose pore size is about $1/49$ of the channel half height δ. Further assume at least five grid points must be used to resolve the pore (in each parallel direction, i.e., x and z) and the same pore spacing, then a well-resolved simulation would require about 5 times of the points in x and 2 times of the points in z as compared to the current simulation, not including the points required to resolve the interior of cavities and pores. The current calculations are computationally intensive due to the nonzero wall-normal velocities caused by porosity near the IBC, creating rather constraining convective CFL conditions. For example, the current grid size for the case $M_b = 3.50$, $R = 0.50$ is $340 \times 300 \times 300$ and one flow-through requires 137143 CPU hours. An equivalent pore-resolved simulation would at least need 0.3 billions of grid point at such high speed and definitely way more CPU hours.
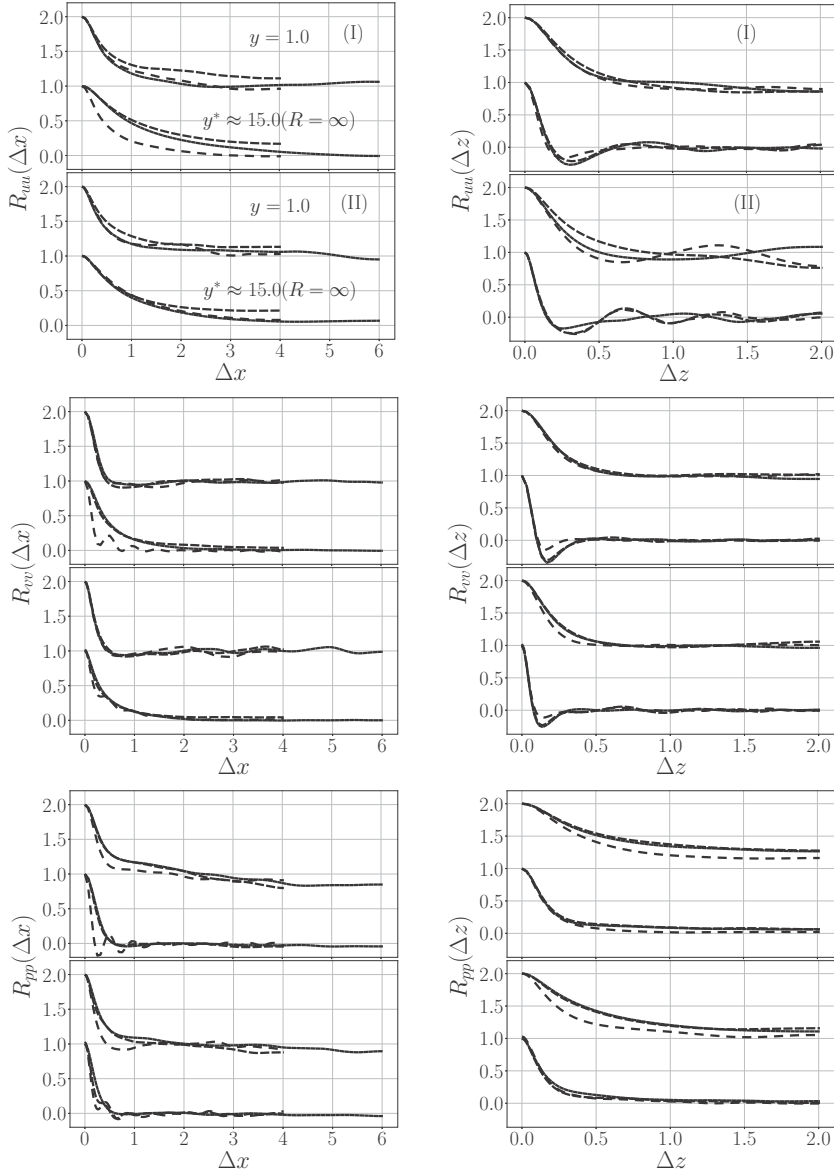
FIG. 9. Two-point correlations in streamwise direction (left column) and spanwise direction (right column) for all cases presented in this work. Variables being evaluated are u, v and p. Two locations are picked: $y^* \approx 15(R = \infty)$ and $y = 1$ (channel center). Note that for impermeable wall cases ($R = \infty$), the domains are longer in streamwise direction as compared to permeable wall cases.

APPENDIX B: TWO-POINT CORRELATION OF CHANNEL FLOWS

Here the two-point correlations of all cases are presented in Fig. 9, which show sufficient domain length in periodic directions.

APPENDIX C: GRID SENSITIVITY STUDY

The grid sensitivity study is conducted with case $M_b = 3.50$, $R = 0.50$, which exhibits most energetic flow response from permeable wall. Three grids are tested. First and second order mean
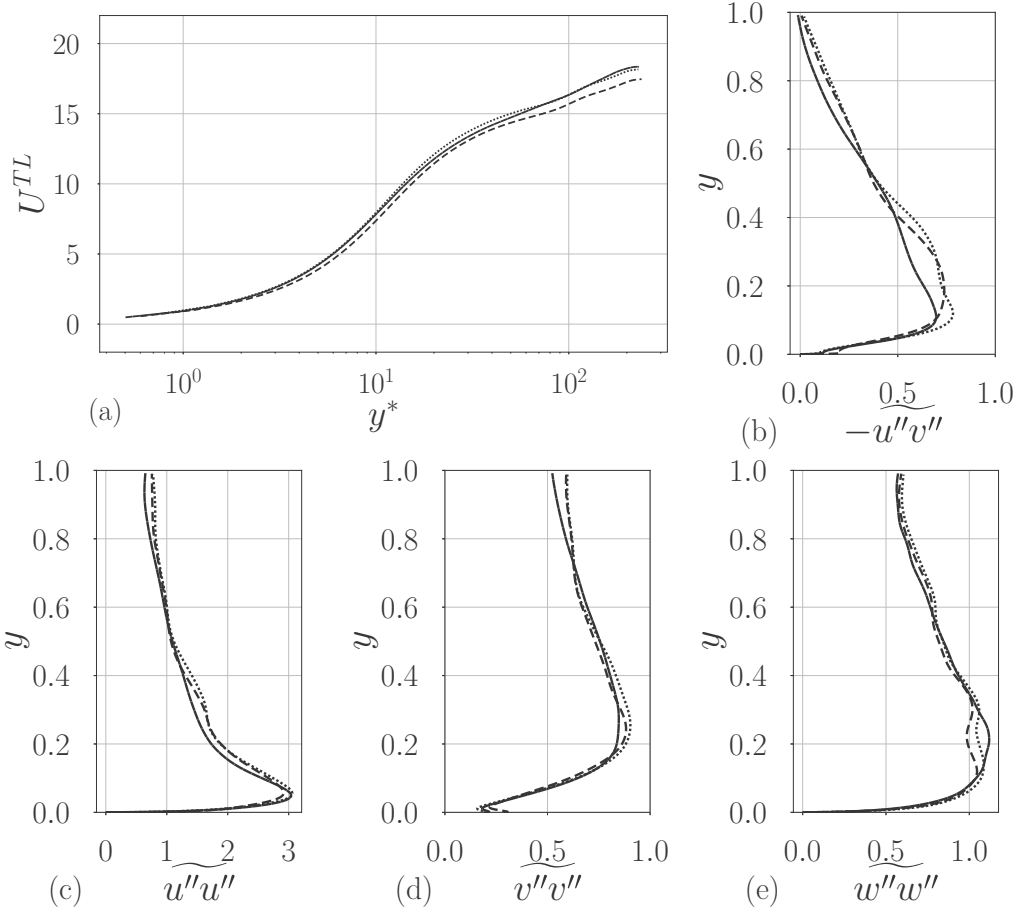
FIG. 10. First and second order statistics of case on different grids of case B2 ($M_b = 3.50, R = 0.50$). Grid sizes presented are: $200 \times 200 \times 180$ (—), $270 \times 256 \times 240$ (—-),$340 \times 300 \times 300$ (—). The quantities shown are (a) mean streamwise velocity in TL-transformation, (b) normalized Reynolds shear stress, (c)–(e) normalized normal stresses. The normalization of the stresses follows the convention $\overline{\rho u_i'' u_j''}/\tau_w$.

flow statistics are plotted in Fig. 10. The mean flow statistics are found to be more sensitive to the grid than impermeable wall cases. Meanwhile the profiles in the outer layer converge much slower than those in the inner layer. The results show decent convergence in the near-wall region, which is the main focus of the current study.

APPENDIX D: TRANSPORT EQUATION OF REYNOLDS STRESS

The derivation of transport equation of Reynolds stress is slightly tedious and is thus omitted here, readers can consult textbooks such as [30]. The result is given as follows with $R_{ij} = \widetilde{u_i'' u_j''}$ denoting the Reynolds stress tensor:

$$\frac{\partial \overline{\rho} R_{ij}}{\partial t} + \frac{\partial \overline{\rho} \widetilde{u}_k R_{ij}}{\partial x_k} = -R_{ik}\frac{\partial \widetilde{u}_i}{\partial x_k} - R_{jk}\frac{\partial \widetilde{u}_j}{\partial x_k} - \epsilon_{ij} + \Pi_{ij} + \frac{\partial}{\partial x_k}[\overline{\tau_{kj}u_i'' + \tau_{ki}u_j''} - C_{ijk}]$$
$$- \overline{u}_i''\frac{\partial P}{\partial x_j} - \overline{u}_j''\frac{\partial P}{\partial x_i}, \tag{D1}$$

where

$$\epsilon_{ij} = \overline{\tau_{kj} \frac{\partial u_i''}{\partial x_k} + \tau_{ki} \frac{\partial u_j''}{\partial x_k}}, \quad \Pi_{ij} = \overline{p'\left(\frac{\partial u_i''}{\partial x_j} + \frac{\partial u_j''}{\partial x_i}\right)}, \quad C_{ijk} = \overline{\rho u_i'' u_j'' u_k''} + \overline{p' u_i''}\delta_{jk} + \overline{p' u_j''}\delta_{ik}. \quad (D2)$$

Equations for the normal stresses can be obtained by simply setting $i = j$.

---

[1] L. E. Kinsler, A. R. Frey, A. B. Coppens, and J. V. Sanders, in *Fundamentals of Acoustics*, 4th ed., edited by Lawrence E. Kinsler, Austin R. Frey, Alan B. Coppens, and James V. Sanders (Wiley-VCH, Weinheim, Germany, 1999), p. 560.

[2] S. Rienstra, Impedance models in time domain, including the extended helmholtz resonator model, in *Proceedings of the 12th AIAA/CEAS Aeroacoustics Conference (27th AIAA Aeroacoustics Conference)* (AIAA, Cambridge, MA, 2006), p. 2686.

[3] Q. Douasbin, C. Scalo, L. Selle, and T. Poinsot, Delayed-time domain impedance boundary conditions (D-TDIBC), J. Comput. Phys. **371**, 50 (2018).

[4] C. K. W. Tam and L. Auriault, Time-domain impedance boundary conditions for computational aeroacoustics, AIAA J. **34**, 917 (1996).

[5] K. Y. Fung and H. Ju, Broadband time-domain impedance models, AIAA J. **39**, 1449 (2001).

[6] D. Dragna, P. Pineau, and P. Blanc-Benon, A generalized recursive convolution method for time-domain propagation in porous media, J. Acoust. Soc. Am. **138**, 1030 (2015).

[7] R. M. Joseph, S. C. Hagness, and A. Taflove, Direct time integration of Maxwell's equations in linear dispersive media with absorption for scattering and propagation of femtosecond electromagnetic pulses, Opt. Lett. **16**, 1412 (1991).

[8] Y. Özyörük and L. N. Long, A time-domain implementation of surface acoustic impedance condition with and without flow, J. Comput. Acou. **5**, 277 (1997).

[9] Y. Özyörük, L. N. Long, and M. G. Jones, Time-domain numerical simulation of a flow-impedance tube, J. Comput. Phys. **146**, 29 (1998).

[10] W. Polifke and C. Wall, Nonreflecting boundary conditions for acoustic transfer matrix estimation with LES, in *Proceedings of the Summer Program 2002* (Center for Turbulence Research, Stanford, CA, 2002), pp. 345–356.

[11] W. Polifke, C. Wall, and P. Moin, Partially reflecting and non-reflecting boundary conditions for simulation of compressible viscous flow, J. Comput. Phys. **213**, 437 (2006).

[12] R. Kaess, A. Huber, and W. Polifke, A time-domain impedance boundary condition for compressible turbulent flow, in *Proceedings of the 14th AIAA/CEAS Aeroacoustics Conference (29th AIAA Aeroacoustics Conference)* (AIAA, Vancouver, British Columbia, Canada, 2008), p. 2921.

[13] J. Jiménez, M. Uhlmann, A. Pinelli, and G. Kawahara, Turbulent shear flow over active and passive porous surfaces, J. Fluid Mech. **442**, 89 (2001).

[14] C. Scalo, J. Bodart, and S. K. Lele, Compressible turbulent channel flow with impedance boundary conditions, Phys. Fluids **27**, 035107 (2015).

[15] R. Sebastian, D. Marx, and V. Fortuné, Numerical simulation of a turbulent channel flow with an acoustic liner, J. Sound Vib. **456**, 306 (2019).

[16] Y. Chen and C. Scalo, Trapped waves in supersonic and hypersonic turbulent channel flow over porous walls, J. Fluid Mech. **920**, A24 (2021).

[17] P. Huang, G. Coleman, and P. Bradshaw, Compressible turbulent channel flows: DNS results and modelling, J. Fluid Mech. **305**, 185 (1995).

[18] A. W. Vreman, An eddy-viscosity subgrid-scale model for turbulent shear flow: Algebraic theory and applications, Phys. Fluids **16**, 3670 (2004).

[19] A. Fedorov, A. Shiplyuk, A. Maslov, E. Burov, and N. Malmuth, Stabilization of a hypersonic boundary layer using an ultrasonically absorptive coating, J. Fluid Mech. **479**, 99 (2003).

[20] T. J. Poinsot and S. K. Lele, Boundary conditions for direct simulations of compressible viscous flows, J. Comput. Phys. **101**, 16 (1992).

[21] J. Lin, C. Scalo, and L. Hesselink, High-Fidelity Simulation of a standing-wave thermoacoustic–piezoelectric engine, J. Fluid Mech. **808**, 19 (2016).

[22] T. Suzuki and S. K. Lele, Green's functions for a source in a boundary layer: Direct waves, channelled waves and diffracted waves, J. Fluid Mech. **477**, 129 (2003).

[23] S. Olivetti, R. D. Sandberg, and B. J. Tester, Direct numerical simulation of turbulent flow with an impedance condition, J. Sound Vib. **344**, 28 (2015).

[24] S. Nagarajan, S. Lele, and J. Ferziger, A robust high-order compact method for large eddy simulation, J. Comput. Phys. **191**, 392 (2003).

[25] R. M. Beam and R. F. Warming, An implicit finite-difference algorithm for hyperbolic systems in conservation-law form, J. Comput. Phys. **22**, 87 (1976).

[26] R. M. Beam and R. Warming, An implicit factored scheme for the compressible Navier-Stokes equations, AIAA J. **16**, 393 (1978).

[27] T. H. Pulliam and D. Chaussee, A diagonal form of an implicit approximate-factorization algorithm, J. Comput. Phys. **39**, 347 (1981).

[28] P. Spalart, Hybrid RKW3 + Crank-Nicolson scheme, internal report (NASA-Ames Research Center, Moffett Field, CA, 1987).

[29] A. Trettel and J. Larsson, Mean velocity scaling for compressible wall turbulence with heat transfer, Phys. Fluids **28**, 026102 (2016).

[30] D. C. Wilcox, *Turbulence Modeling for CFD*, 3rd ed. (DCW industries, La Canada, CA, 1998).

[31] R. D. Ulerich, Reducing turbulence-and transition-driven uncertainty in aerothermodynamic heating predictions for blunt-bodied reentry vehicles, Ph.D. thesis, University of Texas at Austin, 2014.

[32] M. Lee and R. D. Moser, Direct numerical simulation of turbulent channel flow up to $\mathrm{Re}_\tau = 5200$, J. Fluid Mech. **774**, 395 (2015).

[33] S. Pope, *Turbulent flows* (Cambridge University Press, Cambridge, UK, 2000).

[34] J. C. R. Hunt, A. A. Wray, and P. Moin, Eddies, streams and convergence zones in turbulent flow, in *Proceedings of the 1988 Summer Program, NASA/Sanford Center for Turbulence Research* (Center for Turbulence Research, Stanford University, 1988), pp. 193–208.

[35] S. W. Rienstra, A classification of duct modes based on surface waves, Wave Motion **37**, 119 (2003).

[36] P. Cobelli, V. Pagneux, A. Maurel, and P. Petitjeans, Experimental study on water-wave trapped modes, J. Fluid Mech. **666**, 445 (2011).

[37] J. Kim, P. Moin, and R. Moser, Turbulence statistics in fully developed channel flow at low Reynolds number, J. Fluid Mech. **177**, 133 (1987).

[38] M. Cho, Y. Hwang, and H. Choi, Scale interactions and spectral energy transfer in turbulent channel flow, J. Fluid Mech. **854**, 474 (2018).

[39] S. Karl, Numerical investigation of a generic scramjet configuration, Ph.D. thesis, Dresden University of Technology, 2011.

[40] J. Larsson, S. Laurence, I. Bermejo-Moreno, J. Bodart, S. Karl, and R. Vicquelin, Incipient thermal choking and stable shock-train formation in the heat-release region of a scramjet combustor. Part II: Large eddy simulations, Combust. Flame **162**, 907 (2015).

[41] V. C. B. Sousa, D. Patel, J.-B. Chapelier, V. Wartemann, A. Wagner, and C. Scalo, Numerical investigation of second-mode attenuation over carbon/carbon porous surfaces, J. Spacecr. Rockets **56**, 319 (2019).